

## Second-order topological insulator in van der Waals heterostructures of $\text{CoBr}_2/\text{Pt}_2\text{HgSe}_3/\text{CoBr}_2$

Zheng Liu,<sup>1</sup> Yafei Ren<sup>1,2</sup>, Yulei Han<sup>1,3</sup>, Qian Niu,<sup>1</sup> and Zhenhua Qiao<sup>1,4,\*</sup>

<sup>1</sup>CAS Key Laboratory of Strongly-Coupled Quantum Matter Physics, and Department of Physics, University of Science and Technology of China, Hefei, Anhui 230026, China

<sup>2</sup>Department of Materials Science and Engineering, University of Washington, Seattle, Washington 98195, USA

<sup>3</sup>Department of Physics, Fuzhou University, Fuzhou, Fujian 350108, China

<sup>4</sup>ICQD, Hefei National Research Center for Physical Sciences at Microscale, University of Science and Technology of China, Hefei, Anhui 230026, China

 (Received 28 January 2022; revised 30 October 2022; accepted 31 October 2022; published 9 November 2022)

The second-order topological insulator, which has  $(d - 2)$ -dimensional topological hinge or corner states, has been observed in three-dimensional materials, but has yet not been observed in a two-dimensional system. In this work we theoretically propose the realization of a second-order topological insulator in the van der Waals heterostructure of  $\text{CoBr}_2/\text{Pt}_2\text{HgSe}_3/\text{CoBr}_2$ .  $\text{Pt}_2\text{HgSe}_3$  is a large gap  $\mathbb{Z}_2$  topological insulator. With an in-plane exchange field from neighboring  $\text{CoBr}_2$ , a large global band gap of above 70 meV opens up at the edge. The corner states, which are robust against edge disorders and irregular shapes, are confirmed in the nanoflake. We further show that the second-order topological states can also be realized in the heterostructure of the jacutingaite family  $\mathbb{Z}_2$  topological insulators. We believe that our work will be beneficial for the experimental realization of second-order topological insulators in van der Waals layered materials.

DOI: [10.1103/PhysRevB.106.195303](https://doi.org/10.1103/PhysRevB.106.195303)

### I. INTRODUCTION

The second-order topological insulator [1–26] is a kind of topological state of matter that possesses zero-dimensional (0D) corner or one-dimensional (1D) hinge states for a two-dimensional (2D) or three-dimensional (3D) system, respectively. Since it was first conceptually proposed [2,3], second-order topological insulators have been widely studied in the aspects of lattices [4–7], symmetries [8–14], model constructions [15–23], and topological classifications [24,25]. Inspired by these proposals, some potential applications of second-order topological insulators were proposed [27,28]. So far, second-order topological insulators have only been experimentally realized in 3D materials, i.e., bismuth [29],  $\text{Bi}_4\text{Br}_4$  [30]. In 2D, material candidates of second-order topological insulators are still limited [31–37], and the material realization of second-order topological insulators in electronic systems is still rare, which greatly limits the potential development of this field. Therefore, it is highly desirable to explore new material candidates and scalable methods for the 2D second-order topological insulator.

To design a second-order topological state, breaking specified symmetry in first-order topological insulators is a scalable scheme [22], which is believed to be easily implemented by applying external pressure or introducing magnetization. Recently some predictions have been made in 3D systems such as  $\text{SnTe}$  [8],  $\text{EuIn}_2\text{As}_2$  [38], and  $\text{Sm}$ -doped  $\text{Bi}_2\text{Se}_3$  [39]. In the 2D system, the only prediction is made in bismuthene deposited on a bulk magnetic insulator that provides in-plane

magnetization as the symmetry breaking term [37]. However, no experimental progress has been made in this material system. Compared to the heterostructure of a bulk magnetic substrate, the van der Waals (vdW) heterostructure [40,41] constructed by 2D magnetic layers can avoid the cleaved surface problem, which makes it experimentally friendly.

In this work we show the possibility of realizing the second-order topological insulators in the vdW heterostructure of  $\text{CoBr}_2/\text{Pt}_2\text{HgSe}_3/\text{CoBr}_2$  with large band gap and robust corner states. In the absence of spin-orbit coupling (SOC), the magnetic proximity effect leads to a considerable spin splitting at valleys  $K$  and  $K'$ . When the SOC is considered, sizable bulk and nanoribbon band gaps are opened. In the nanoflake, one topological corner state arises at the intersection of boundaries with its eigenenergy being located inside the energy gap of edge states (see Fig. 10 for the schematics of the nanoribbon and nanoflake). When irregular boundary and Anderson disorders are introduced, we show that the topological corner states are almost unaffected. Besides  $\text{Pt}_2\text{HgSe}_3$ , we find that other  $\mathbb{Z}_2$  topological insulators of the jacutingaite family can also be utilized as the candidate materials for the realization of topological corner states. Moreover, a low-energy effective model based on topological edge states is constructed, demonstrating that the 1D Jackiw-Rebbi model can be used to explain the presence of topological corner states.

### II. CALCULATION METHODS AND ATOMIC STRUCTURE

Our first-principles calculations were performed by using the projected augmented-wave method [42] as implemented in the Vienna *ab initio* simulation package (VASP) [43].

\*Corresponding author: [qiao@ustc.edu.cn](mailto:qiao@ustc.edu.cn)

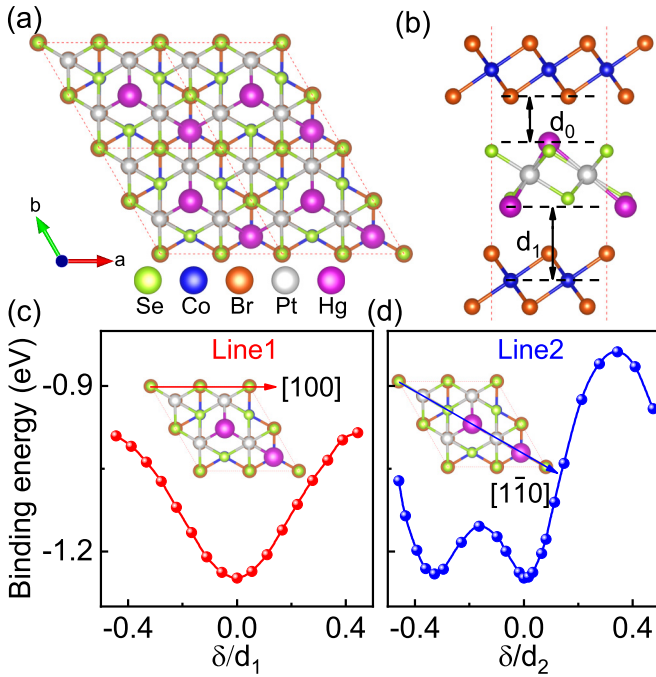


FIG. 1. (a) and (b) Top and side views of the heterostructures of  $\text{CoBr}_2/\text{Pt}_2\text{HgSe}_3/\text{CoBr}_2$ . (c) and (d) Binding energies along the high symmetry lines for the respective horizontal and diagonal directions. Here  $\delta$  represents the displacement, and  $d_1$  and  $d_2$  are half the length of the lattice constants of horizontal and diagonal directions.

The generalized gradient approximation of the Perdew-Burke-Ernzerhof type was used to describe the exchange-correlation interaction [44]. All atoms were allowed to relax until the Hellmann-Feynman force on each atom is smaller than 0.01 eV/Å. The  $\Gamma$ -centered Monkhorst-Pack grid of  $7 \times 7 \times 1$  was carried out in all our calculations. For the Co, the GGA+ $U$  method was used with the on-site repulsion energy  $U = 3.67$  eV [45]. The vdW interaction was treated by using the DFT-D2 functional [46]. And the topological properties were calculated by using maximally localized Wannier functions as implemented in the Wannier90 package [47]. A vacuum buffer layer of 20 Å was used to avoid interaction between adjacent slabs. The plane-wave energy cutoff was set to be 400 eV.

Figures 1(a) and 1(b) display the heterostructure of  $\text{CoBr}_2/\text{Pt}_2\text{HgSe}_3/\text{CoBr}_2$ , where 3D bulk  $\text{Pt}_2\text{HgSe}_3$  is a dual-topological semimetal that can be exfoliated down to a few layers in ambient conditions [48–51], monolayer  $\text{Pt}_2\text{HgSe}_3$  is a  $\mathbb{Z}_2$  topological insulator with a large band gap of 0.17 eV [52,53], and monolayer  $\text{CoBr}_2$  is a ferromagnetic insulator with an in-plane magnetic easy axis [45]. The lattice constants are 7.35 Å for  $\text{Pt}_2\text{HgSe}_3$  and 3.71 Å for the  $\text{CoBr}_2$  monolayer, thus we slightly compress the  $2 \times 2$   $\text{CoBr}_2$  supercell to match the  $\text{Pt}_2\text{HgSe}_3$  monolayer during the calculation. We find that the main properties of the heterostructure are not obviously affected by small lattice stretch or compression (see Fig. 11).

The structural stability is strictly checked by calculating the binding energy of  $\text{Pt}_2\text{HgSe}_3/\text{CoBr}_2$  heterostructure with a series of different stacking configurations. The binding energy can be expressed as  $\Delta E = E_H - E_P - E_C$ , where  $E_H$ ,  $E_P$ , and

$E_C$  are, respectively, the total energy of the heterostructure,  $\text{Pt}_2\text{HgSe}_3$  monolayer, and  $\text{CoBr}_2$  monolayer. As shown in Figs. 1(c) and 1(d), the calculated binding energies suggest that the bottom Hg atoms prefer to sit on top of the Co atoms. And the energy barrier is as large as tens of millielectron volts as we shift the  $\text{Pt}_2\text{HgSe}_3$  monolayer away from its most stable stacking structure. Here we only discuss electronic and topological properties of the most stable configuration as shown in Figs. 1(a) and 1(b). The possible fabrication method and thermodynamic stability of the heterostructure are discussed in Appendix B.

### III. LOW-ENERGY EFFECTIVE MODEL OF THE HETEROSTRUCTURE

Before demonstrating detailed first-principles calculation results, it is necessary to clearly illustrate the underlying physics. As reported in previous studies [52,53],  $\text{Pt}_2\text{HgSe}_3$  is a Kane-Mele type topological insulator, which exhibits two Dirac cones at  $K$  and  $K'$  as graphene in the absence of SOC and opens a large band gap at the Dirac points after considering SOC. By calculating the band structure evolution of the heterostructure, we find that  $\text{CoBr}_2$  covering layers provide sizable in-plane magnetization to  $\text{Pt}_2\text{HgSe}_3$  but have negligible orbital contributions around the Fermi level. To capture the essential topological properties and band shapes around the Fermi level, a low-energy effective model at  $K$  and  $K'$  valleys is constructed as follows [52–57]:

$$H = H_0 + H_{\text{soc}} + H_m, \quad (1)$$

where  $H_0 + H_{\text{soc}}$  describes the electronic properties of  $\text{Pt}_2\text{HgSe}_3$  with  $H_0 = \hbar v_F(\tau_z \sigma_x k_x + \sigma_y k_y) s_0$  characterizing the Dirac dispersion around  $K/K'$  valleys and  $H_{\text{soc}} = \lambda_0 \tau_z \sigma_z s_z$  representing the SOC.  $\tau$ ,  $\sigma$ , and  $s$  are Pauli matrices for the valley, sublattice, and spin, respectively.  $H_m = m_0 s_y$  represents the in-plane magnetization provided by  $\text{CoBr}_2$  layers. The evolution properties of the low-energy effective model is the same with the *ab initio* results (see Appendix C), indicating the former can capture the essential topological properties of the heterostructure.

In the presence of in-plane magnetization, the bulk band structure becomes split upward (downward) when the  $s_y$  eigenvalue equals +1 (−1), respectively, as displayed as dashed lines of Fig. 2(a). When the SOC is further included, four anticrossings occur at the bands with opposite spin directions as the SOC can mix up the  $s_y = \pm 1$  eigenstates.

### IV. LOW-ENERGY EFFECTIVE MODEL OF THE EDGE STATES

To clearly understand the second-order topological state, we construct a low-energy effective model on the basis of the topological edge states that gives the edge-corner correspondence, just like the bulk-edge correspondence in first-order topological insulators. In the following we show the details in the establishment of the low-energy effective model of the edge states. We mapped the bulk low-energy effective model to the honeycomb lattice and a full numerical method was used during the construction. The corresponding real-space

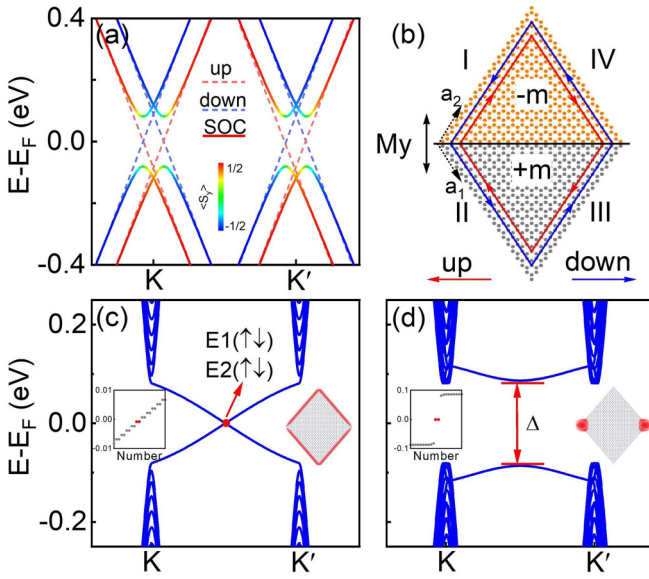


FIG. 2. (a) The band structure of an in-plane magnetized hexagonal lattice without (dashed line) and with (solid line) SOC. The color of the solid line represents the expectation value of the  $s_y$  operator. (b) The schematic diagram of spin up/down edge states and mass term when in-plane magnetization is induced. (c) and (d) The band structure of a zigzag nanoribbon without (c) and with (d) in-plane magnetization, respectively. The insets in (c) and (d) show the energy spectrums of the 0D nanoflake and the probability distribution of the states marked in red.

Hamiltonian in the honeycomb lattice can be expressed as

$$H = t \sum_{\langle ij \rangle \alpha} c_{i\alpha}^\dagger c_{j\alpha} + i\lambda_{\text{soc}} \sum_{\langle\langle ij \rangle\rangle \alpha\beta} v_{ij} s_{\alpha\beta}^z c_{i\alpha}^\dagger c_{j\beta} + \sum_{i\alpha\beta} m_0 s_{\alpha\beta}^y c_{i\alpha}^\dagger c_{i\beta}, \quad (2)$$

where  $c_{i\alpha}^\dagger$  ( $c_{i\alpha}$ ) is the creation (annihilation) operator for an electron on site  $i$  with spin  $\alpha$ .  $v_{ij} = \mathbf{d}_j \times \mathbf{d}_i / |\mathbf{d}_j \times \mathbf{d}_i|$ , where  $\mathbf{d}_i$  and  $\mathbf{d}_j$  are two nearest neighbor bonds connecting the next-nearest neighbor sites. The hopping amplitude and SOC strength are given by  $t = \frac{2}{\sqrt{3}} \hbar v_F$  and  $\lambda_{\text{soc}} = \frac{1}{3\sqrt{3}} \lambda_0$ , respectively.

### A. Effective model of edge states in the absence of magnetization

We consider a zigzag nanoribbon which is periodic in  $x$  direction and finite in  $y$  direction as shown in Fig. 3. The Hamiltonian of the nanoribbon can be expressed as  $H(k_x) = H^0 + H^1 k_x + H_m$  where the insignificant  $k_x^n$  ( $n \geq 2$ ) terms have been omitted. Here we refer to  $H_0$  as the unperturbed Hamiltonian and other terms as perturbations. Numerically solving the eigenvalue problem of  $H^0$ , we find fourfold degenerate edge states which can be expressed as  $|E_{1\uparrow}\rangle$ ,  $|E_{1\downarrow}\rangle$ ,  $|E_{2\uparrow}\rangle$ , and  $|E_{2\downarrow}\rangle$  with  $E_1$  ( $E_2$ ) corresponding to edges and arrows representing the spin. In the absence of in-plane magnetization, by treating  $H^1 k_x$  as a perturbation, the effective model of the edge  $E_1$  can be written as

$$H_{E_1} = \begin{pmatrix} \langle E_{1\uparrow} | H^1 k_x | E_{1\uparrow} \rangle & \langle E_{1\uparrow} | H^1 k_x | E_{1\downarrow} \rangle \\ \langle E_{1\downarrow} | H^1 k_x | E_{1\uparrow} \rangle & \langle E_{1\downarrow} | H^1 k_x | E_{1\downarrow} \rangle \end{pmatrix}. \quad (3)$$

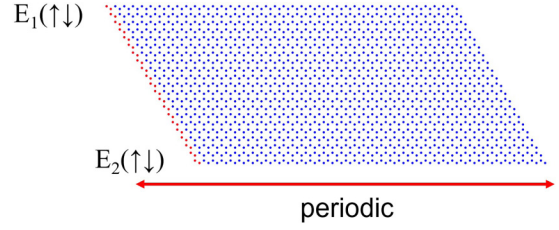


FIG. 3. The lattice structure of the nanoribbon with its unit cell marked in red. As the nanoribbon is periodic in  $x$  direction and finite in  $y$  direction, zero-energy edge states exist at the two edges  $E_1$  and  $E_2$ .

Numerically calculating the matrix elements, the effective model of edge states can be expressed as

$$H_{\text{edge}} = -\eta v_0 k_x \sigma_z, \quad (4)$$

with  $\eta = +1$  ( $-1$ ) for edges  $E_1$  and  $E_2$ , respectively. The effective model shows that the spin up and spin down electrons move along opposite directions at the edges which manifests the nature of the  $\mathbb{Z}_2$  topological insulator.

### B. Effective model of edge states with in-plane magnetization

In the presence of in-plane magnetization, the spin up and spin down edge states will mix with each other, thus an energy gap will be opened. Using the perturbation method, we can well explain the gap open mechanism. When the in-plane magnetization is included, the perturbation term is  $H^1 k_x + H_m$  with  $H_m = m_0 s_y$ . The low-energy effective model for the in-plane magnetization term  $H_m$  can be expressed as

$$H_{m,E_1} = \begin{pmatrix} \langle E_{1\uparrow} | H_m | E_{1\uparrow} \rangle & \langle E_{1\uparrow} | H_m | E_{1\downarrow} \rangle \\ \langle E_{1\downarrow} | H_m | E_{1\uparrow} \rangle & \langle E_{1\downarrow} | H_m | E_{1\downarrow} \rangle \end{pmatrix}. \quad (5)$$

Calculating the matrix elements, we find that different from the effective model of  $H^1 k_x$ , which only has the diagonal terms, the effective model for the in-plane magnetization term only has off-diagonal terms which is

$$H_{m,E_1} = \begin{pmatrix} 0 & \alpha m \\ \alpha^* m & 0 \end{pmatrix}, \quad (6)$$

where  $\alpha$  is a complex number with  $|\alpha| = 1$  which comes from the undetermined phase difference between edge states  $|E_{1,\uparrow}\rangle$  and  $|E_{1,\downarrow}\rangle$ . The total effective model for edge  $E_1$  can be expressed as

$$H_{\text{eff},E_1} = \begin{pmatrix} v_0 k_x & \alpha m \\ \alpha^* m & -v_0 k_x \end{pmatrix}. \quad (7)$$

By using the same way, the effective model of edge  $E_2$  can be written as

$$H_{\text{eff},E_2} = \begin{pmatrix} -v_0 k_x & \beta m \\ \beta^* m & v_0 k_x \end{pmatrix}, \quad (8)$$

where  $|\beta| = 1$ .

We find that the energy dispersion of the low-energy effective model is

$$\epsilon_{k_x}^\pm = \pm \sqrt{v_0^2 k_x^2 + m^2}. \quad (9)$$

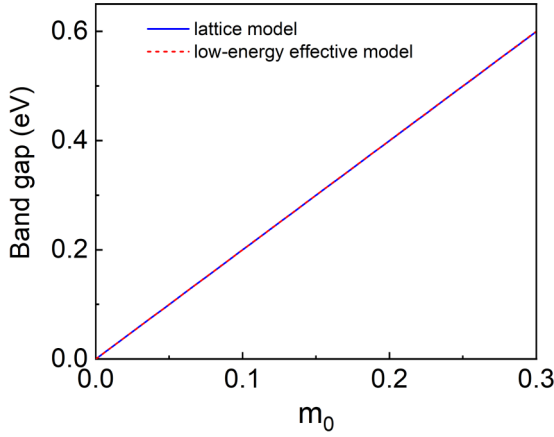


FIG. 4. The edge band gap as a function of in-plane magnetization coefficient  $m_0$  for the lattice model and low-energy effective model.

The energy spectrum shows that a band gap of  $\Delta = 2m$  is opened by in-plane magnetization at the edges. More importantly, the low-energy effective model can well capture the band opening process. As shown in Fig. 4, the calculated band gaps of the lattice model and low-energy effective model have the same values, indicating that our effective model can well describe the edge band gap.

### C. Effective mass term of edges in a 0D nanoflake

Previous results show that in-plane magnetization will induce an effective mass term which can open a gap in the energy spectrum of the edge. However, the undetermined phase factors  $\alpha$  and  $\beta$  block the determination of the mass terms of edges. To solve this problem, we consider the edge states in a 0D nanoflake in which the phase factors of edges are locked.

As shown in Fig. 5(a), we plot the energy spectrum of the nanoflake without in-plane magnetization. Because of the existence of time reversal symmetry, the eigenstates are doubly degenerate. As the commutation relation  $[H_0 + H_{\text{soc}}, s_z] = 0$  is preserved, the doubly degenerate states can be separated to spin up and spin down states which are expressed as  $\psi_\uparrow$  and

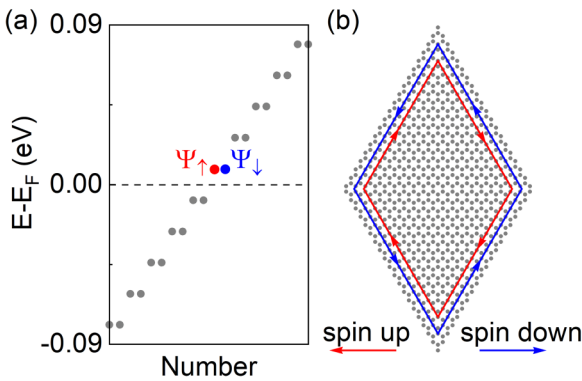


FIG. 5. (a) The energy spectrum of the zero-dimensional nanoflake. (b) The conducting channels of the spin up and spin down edge states.

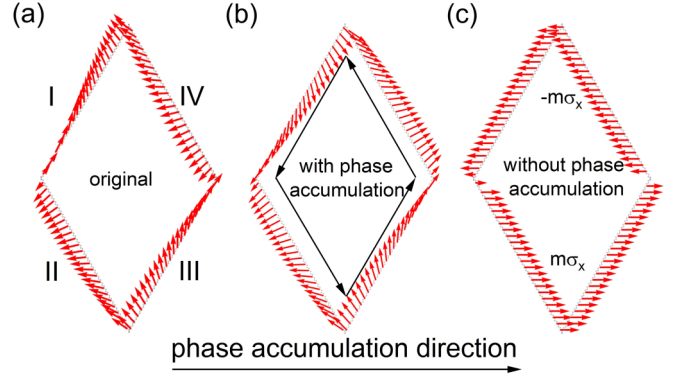


FIG. 6. The illustration of vector  $\mathbf{n}$  at edges of the nanoflake. (a) The original result gotten from the spin up and spin down wave functions. (b) The evaluation of vector  $\mathbf{n}$  from the phase factors accumulation of a finite momentum  $k$ . (c) The remaining part of vector  $\mathbf{n}$  by eliminating the phase factors accumulation.

$\psi_\downarrow$ , respectively. As discussed previously, the two eigenstates move in opposite directions as illustrated in Fig. 5(b). By using the numerical edge states  $\psi_\uparrow$  and  $\psi_\downarrow$ , we can get the effective mass term on every atom site. Seeing the in-plane magnetization  $H_m$  as a perturbation, the mass term on each atom site can be expressed as

$$H'_{\text{eff},i} = \begin{pmatrix} \langle \psi_{\uparrow,i} | H_m | \psi_{\uparrow,i} \rangle & \langle \psi_{\uparrow,i} | H_m | \psi_{\downarrow,i} \rangle \\ \langle \psi_{\downarrow,i} | H_m | \psi_{\uparrow,i} \rangle & \langle \psi_{\downarrow,i} | H_m | \psi_{\downarrow,i} \rangle \end{pmatrix}, \quad (10)$$

with  $\psi_{\uparrow,i}$  and  $\psi_{\downarrow,i}$  representing the spin up and spin down wave functions at site  $i$ , which are two-dimensional column vectors. Seeing the effective mass term as a pseudospin, we have

$$H'_{\text{eff},i} = \mathbf{n} \cdot \boldsymbol{\sigma}, \quad (11)$$

with  $\mathbf{n}$  representing the magnitude and direction of the effective mass term. By calculating the matrix elements of  $H'_{\text{eff},i}$ , we can get the vector  $\mathbf{n}$  and its angle as plotted in Fig. 6(a). Note that, vector  $\mathbf{n}$  always stays in the  $xy$  plane as the diagonal parts of  $H'_{\text{eff},i}$  are zero. We can see that the vector  $\mathbf{n}$  continuously evolves along the I, IV or II, III edges while sharply inverses its direction at the corners between I/II and III/IV edges which indicates the sign change of the mass term across those corners.

To see it more clearly, we separate the vector  $\mathbf{n}$  into two parts: (1) The phase factor from a finite momentum  $k$  [as shown in Fig. 6(b)]. (2) The remaining part by eliminating the continuous phase accumulation [as shown in Fig. 6(c)]. The continuous evolution of vector  $\mathbf{n}$  origins from the phase factors accumulated by the spin up and spin down states as they move away from their initial positions. As the spin up and spin down states move along opposite directions (illustrated in Fig. 5), the phase accumulations are  $e^{ikl}$  and  $e^{-ikl}$ , respectively, where  $l$  refers to the atomic position and  $k$  represents the finite momentum. This phase accumulation will add a clockwise rotation to vector  $\mathbf{n}$  with angle  $2kl$ . Specifically, the wave function at site  $i$  can be expressed as  $\psi_{\uparrow,i} = e^{ikl} \psi_{\uparrow,i,0}$  and  $\psi_{\downarrow,i} = e^{-ikl} \psi_{\downarrow,i,0}$ , with  $\psi_{\uparrow,i,0}$ ,  $\psi_{\downarrow,i,0}$  representing the states which do not introduce the phase accumulation. Then we have

the relation

$$\begin{pmatrix} n_x \\ n_y \end{pmatrix} = \begin{pmatrix} \cos \theta & \sin \theta \\ -\sin \theta & \cos \theta \end{pmatrix} \begin{pmatrix} n_{0x} \\ n_{0y} \end{pmatrix}, \quad (12)$$

with  $\theta = 2kl$  and  $\mathbf{n}_0$  representing the effective mass term without phase accumulation. We can find that Eq. (12) is the clockwise rotation of the vector  $\mathbf{n}_0$ . As shown in Fig. 6(b), this phase factor goes  $2\pi$  along the boundary. In Fig. 6(c) we plot the remaining part of vector  $\mathbf{n}$  by eliminating the continuous phase accumulation. Vector  $\mathbf{n}$  is in  $-x$  direction at I, IV edges and in  $+x$  direction at II, III edges, indicating that the effective mass term changes its sign at the corners of these edges.

To be more clear, we summarize our main results in Fig. 2(b). The effective model can be rewritten by taking ‘‘edge coordinate’’  $l$  that grows anticlockwisely,

$$H_{\text{eff}} = iv_0\sigma_z\partial_l + m(l)\sigma_x, \quad (13)$$

where  $m(l) = +m$  ( $-m$ ) for edge II and III (I and IV). By applying a unitary transformation  $U = \exp(i\sigma_y\pi/4)$ , Eq. (13) becomes

$$H'_{\text{eff}} = -iv_0\sigma_x\partial_l + m(l)\sigma_z, \quad (14)$$

which is exactly the 1D Jackiw-Rebbi model [58]. Thus, there always exist zero energy solutions near the domain walls, where  $m$  changes its sign. The numerical results are consistent with the effective model. As shown in Figs. 2(c) and 2(d), the edge spectrum is gapped after the presence of in-plane magnetization. When taking the 0D nanoflake into consideration, two zero energy states with a wave function distributed at the corner occur.

## V. BAND STRUCTURES AND SECOND-ORDER TOPOLOGICAL PROPERTIES

The band structure evolution from first-principles calculations agrees well with our model analysis. As shown in Fig. 7(a), the spin majority and spin minority bands are largely separated at  $K/K'$  point when SOC is not included, indicating that  $\text{CoBr}_2$  covering layers provide sizable in-plane magnetization to  $\text{Pt}_2\text{HgSe}_3$ . In the presence of SOC, large band gaps are opened around the band crossing points as illustrated in Fig. 7(b). The spin projections  $\langle s_y \rangle$  show that the  $s_y = +1$  and  $s_y = -1$  states are mixed by SOC which is consistent with the results in our low-energy effective model shown in Fig. 2(a).

To explore the topological properties of the heterostructure, the energy spectra of the 1D nanoribbon and 0D nanoflake are calculated by using the Hamiltonian generated from the maximally localized Wannier functions [47]. The atomic orbitals of Hg ( $s$ ) and Pt ( $d_{xy}, d_{yz}, d_{x^2}, d_{yz}$ ) are used for projection since they contribute dominantly to the energy bands near the Fermi level. In Figs. 7(c) and 7(d) we plot the edge states of the 1D zigzag nanoribbon by using the surface Green’s function technique. Similar to Fig. 2(d), sizable band gaps of edge states are opened in the heterostructure (see more detailed analyses of the edge states band gap and the corresponding model results in Appendix D). To verify the formation of corner states, we calculate the energy spectrum of the nanoflake system with  $40 \times 40$  unit cells. As shown in Fig. 7(e), we find one in-gap state highlighted in red, with its probability density distributed around one corner. When disorders are introduced

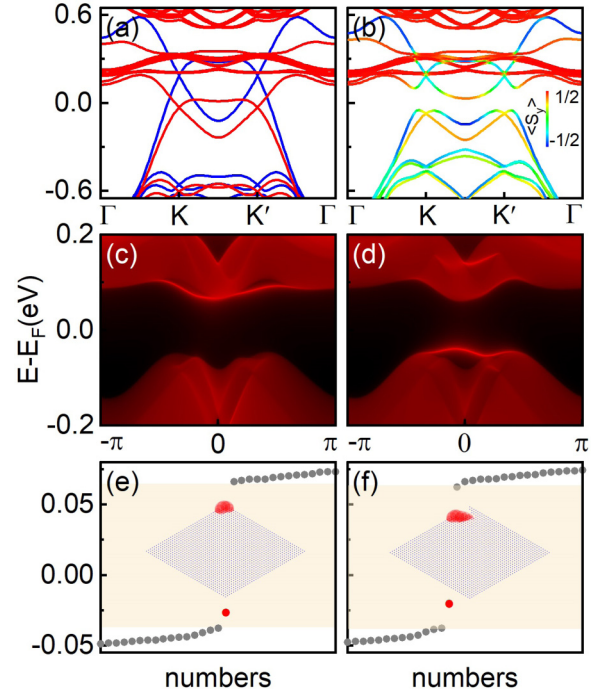


FIG. 7. (a) and (b) Band structure of  $\text{CoBr}_2/\text{Pt}_2\text{HgSe}_3/\text{CoBr}_2$  heterostructure without and with SOC. In (a) the red (blue) represents spin up (down) states. The color of the line represents the expectation value of the  $s_y$  operator in (b). (c) and (d) Edge states of the zigzag nanoribbon with (c) and (d) representing the right and left terminals, respectively. (e) and (f) Energy levels of the nanoflake. Corner states are highlighted in red. The insets show the distribution of the corner state. In (f) the corner state still exists with irregular boundaries.

by introducing edge randomness, we find that the topological corner state still exists at the irregular region [see Fig. 7(f)].

As the upper and lower edges of the 0D nanoflake are constructed by Hg and Pt atoms, respectively (see Fig. 17), different on-site potentials are expected at the edges. Though unequal edge potentials can move the energy levels of the edge states and corner states, the existence of topological corner states are not affected. Similar results were also reported in Sm-doped  $\text{Bi}_2\text{Se}_3$  which is a 3D second-order topological insulator [39]. See Appendix E for detailed analyses of the influence of the edge potential.

## VI. ROBUSTNESS OF THE CORNER STATES

To explore the robustness of the corner states, we add random disorders  $H_d$  to the outermost unit cells, where  $H_d = w \sum_i c_i^\dagger c_i$  with  $w$  being uniformly distributed within an interval of  $[-W/2, W/2]$ . The disorder strength is set as  $W = 80$  meV that is approximately in the same magnitude of the edge band gap. The local density of states (LDOS) around the corner is introduced to characterize the existence of corner states. The LDOS can be calculated by using retarded Green’s function

$$\text{LDOS}(E, n) = -\frac{1}{\pi} \text{Im} \left[ \frac{1}{E - H + i\delta} \right]_{nn}, \quad (15)$$

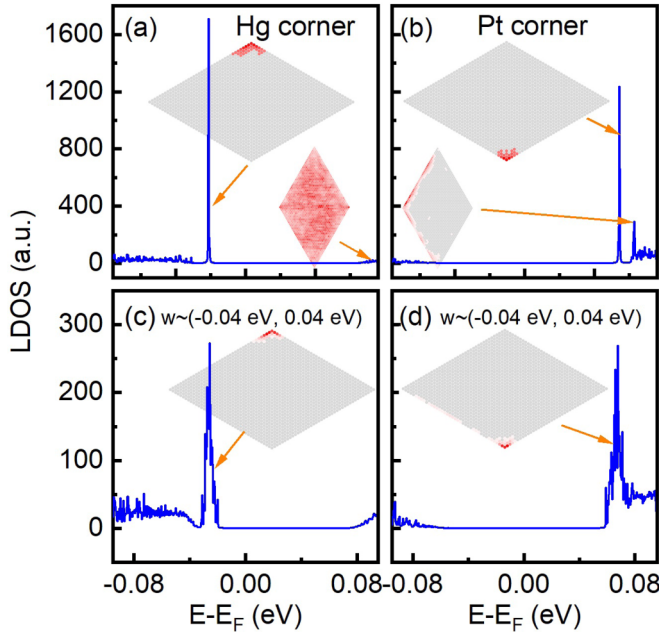


FIG. 8. (a) and (b) Local density of states at Hg and Pt corners, respectively. Insets show the local density of states at real space for the corner, edge, and bulk states at a specific energy. (c) and (d) The average local density of states in the presence of disorder for Hg (c) and Pt (d) corners, respectively. Disorder strength is set as  $W = 80$  meV. Over 100 samples are collected.

where  $n$  represents the atomic site. Figure 8 plots the LDOS summation of atomic sites at three unit cells around the corners with obtuse angles. In the absence of disorder, sharp peaks occur in Figs. 8(a) and 8(b), corresponding to corner states at Hg and Pt edges, respectively. Aside from the typical peaks, LDOS can also provide real-space distributions of electronic states. The electronic states are predominantly localized around the corner at the peaks of the LDOS curve, as illustrated in the inset of Figs. 8(a) and 8(b). When the random disorders are introduced, we plot the averaged LDOS on 100 samples as displayed in Figs. 8(c) and 8(d). One can see that the peaks for corner states are still visible, suggesting that topological corner states are robust against weak disorder.

## VII. CORNER STATES IN THE $\text{Pt}_2\text{HgSe}_3$ FAMILY

To explore the possibility of realizing corner states in other heterostructures of the  $\text{Pt}_2\text{HgSe}_3$  family materials [53,59,60], we systematically study the electronic band structures and topological properties of  $\text{MZ}_2/\text{Pt}_2\text{XS}_3/\text{MZ}_2$  ( $M = \text{Co}$  and  $\text{Ni}$ ;  $Z = \text{Br}$  and  $\text{Cl}$ ;  $X = \text{Zn}$  and  $\text{Hg}$ ). As displayed in Table I, most heterostructures have small lattice mismatch and sizable band gaps. By calculating the energy spectrums and wave function distributions of the nanoflake, three candidates with topological corner states are discovered (see more details in Appendix F).

## VIII. THE DETECTION OF TOPOLOGICAL CORNER MODES

The differential conductance spectra from the scanning tunneling microscope (STM) experiments are proportional to

TABLE I. Structural, band, and topological properties of heterostructures in the  $\text{Pt}_2\text{HgSe}_3$  family.

Heterostructure	Lattice mismatch	Band gap	Second-order TI
$\text{Pt}_2\text{ZnS}_3/\text{CoBr}_2$	4.01%	8.3 meV	No
$\text{Pt}_2\text{ZnS}_3/\text{CoCl}_2$	1.37%	29.4 meV	No
$\text{Pt}_2\text{ZnS}_3/\text{NiBr}_2$	1.68%	0 meV	No
$\text{Pt}_2\text{ZnS}_3/\text{NiCl}_2$	3.14%	24.1 meV	Yes
$\text{Pt}_2\text{HgS}_3/\text{CoBr}_2$	3.78%	58.0 meV	Yes
$\text{Pt}_2\text{HgS}_3/\text{CoCl}_2$	1.60%	88.6 meV	Yes
$\text{Pt}_2\text{HgS}_3/\text{NiBr}_2$	1.45%	62.9 meV	No
$\text{Pt}_2\text{HgS}_3/\text{NiCl}_2$	3.37%	48.9 meV	No

the local density of states (LDOS) which can be used to detect corner states. According to the energy spectrum, we know that the corner states appear in the energy gaps of the edge and bulk states, i.e., the bulk, edge, and corner states can be distinguished at different bias voltages in STM experiments. Specifically, one can compare the differential conductance spectra of the bulk, edge, and corner. For a second-order topological insulator, the peaks corresponding to the corner states exist in the corner spectrum while the edge and bulk spectra do not have these peaks. Besides, it is more efficient to see the real space distributions of corner states by getting the differential conductance maps around the corner at the bias voltage around the peak in the corner spectrum (the eigenvalue of the corner state).

Based on the LDOS map in the insets of Figs. 8(a) and 8(b), the corner states are found in several unit cells of the heterostructure. Thus, the corner states have different features to the electronic states generated by the random disorder which are mainly localized in the atomic size range. As the corner states are topologically protected, if we cut off one corner state, another new corner state will be generated at the newly built corner as illustrated in Fig. 9. This property is the unique feature of the topological corner state which distinguishes it from the topological trivial state and it can be used as strong evidence for confirming the corner state experimentally. Actually, the topological corner state has been experimentally confirmed in an artificial electronic system by using STM recently [61] suggesting the detection is achievable.

## IX. SUMMARY

We demonstrate that the two-dimensional second-order topological states can be realized in the vdW heterostructures

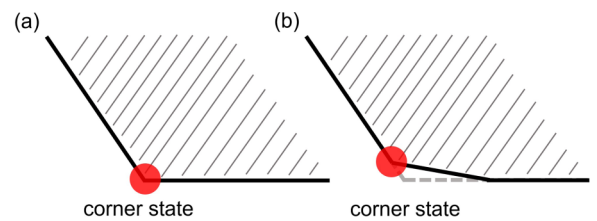


FIG. 9. Illustration of the unique properties of the topological corner states. If we cut off the corner state shown in (a), a new corner state will occur around the newly built corner as shown in (b).

of  $\text{CoBr}_2/\text{Pt}_2\text{HgSe}_3/\text{CoBr}_2$ .  $\text{CoBr}_2$  layers proximity induce a considerable in-plane exchange field in  $\text{Pt}_2\text{HgSe}_3$ , which makes the edge states gapped. Inside the band gap we find corner states in a nanoflake geometry that can be understood by a 1D Jackiw-Rebbi model. We find that the corner states can be probed by measuring the local density of states near the corner, which is robust against the atomic randomness at the boundaries and Anderson disorders. We show that these topological corner states can also be realized in other candidate materials, e.g.,  $\text{MZ}_2/\text{Pt}_2\text{XS}_3/\text{MZ}_2$  ( $M = \text{Co}$  and  $\text{Ni}$ ;  $Z = \text{Br}$  and  $\text{Cl}$ ;  $X = \text{Zn}$  and  $\text{Hg}$ ). The proposed realistic material system for a two-dimensional second-order topological insulator should be significant to experimental realization and inspire further investigation in this field.

### ACKNOWLEDGMENTS

This work was financially supported by the National Natural Science Foundation of China (11974327 and 12004369), Fundamental Research Funds for the Central Universities (Grants No. WK3510000010 and No. WK2030020032), and Anhui Initiative in Quantum Information Technologies (Grant No. AHY170000). We are grateful to AMHPC and Supercomputing Center of USTC for providing the high-performance computing resources.

### APPENDIX A: SCHEMATIC OF THE NANORIBBON AND NONOFLAKE

In Fig. 10 we plot the schematic to illustrate the nanoribbon and nanoflake. The nanoribbon is periodic in one direction while limited in another direction. The nanoflake is diamond shaped.

### APPENDIX B: THE POSSIBLE FABRICATION METHOD AND STABILITY OF THE HETEROSTRUCTURE

We recommend to grow the heterostructure via chemical vapor deposition or molecular-beam epitaxy method. Previous experiments have shown that the high-quality vertically stacked heterostructure with certain stacking order, no lattice mismatch, and no twist angles can be fabricated by the growth method. For example,  $\text{WS}_2/\text{MoS}_2$  heterostructure is epitaxially grown with 2H stacking though the initial lattice constants

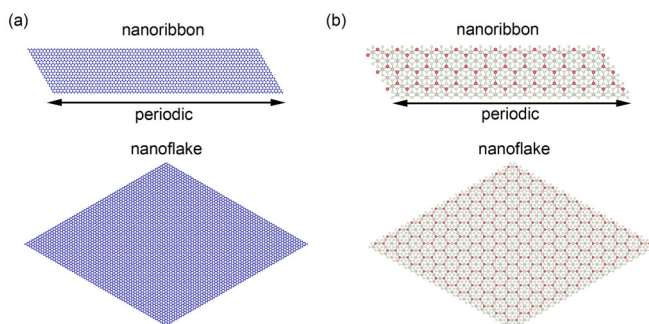


FIG. 10. The schematic of the nanoribbon and nanoflake for the model calculation (a) and  $\text{CoBr}_2/\text{Pt}_2\text{HgSe}_3/\text{CoBr}_2$  heterostructure (b).

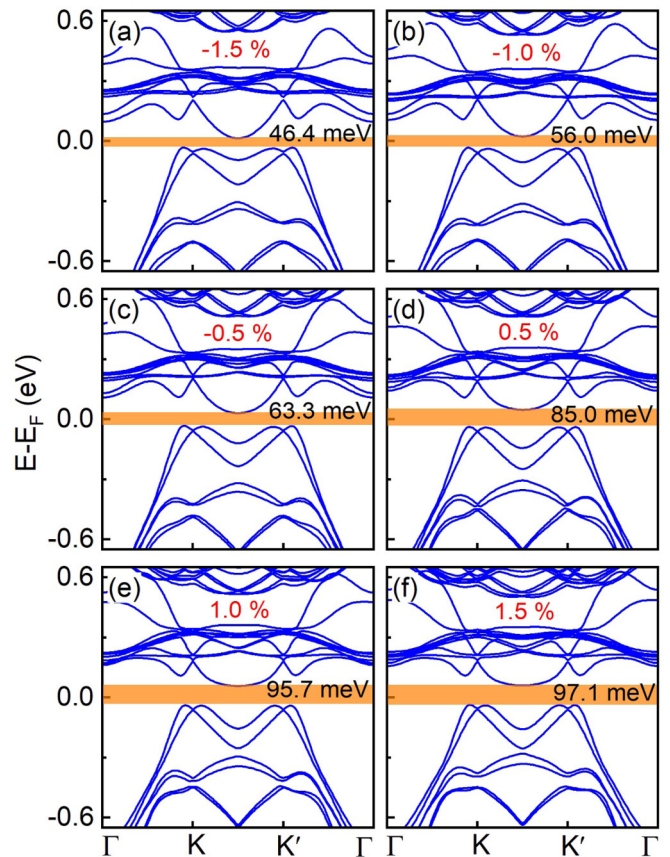


FIG. 11. The band structure of  $\text{CoBr}_2/\text{Pt}_2\text{HgSe}_3/\text{CoBr}_2$  heterostructures in the presence of compressive and tensile stress with lattice parameters changing from  $-1.5\%$  to  $1.5\%$ .

of the two monolayer materials are different [62,63]. Actually, many van der Waals heterostructures have been successfully grown [64–67].

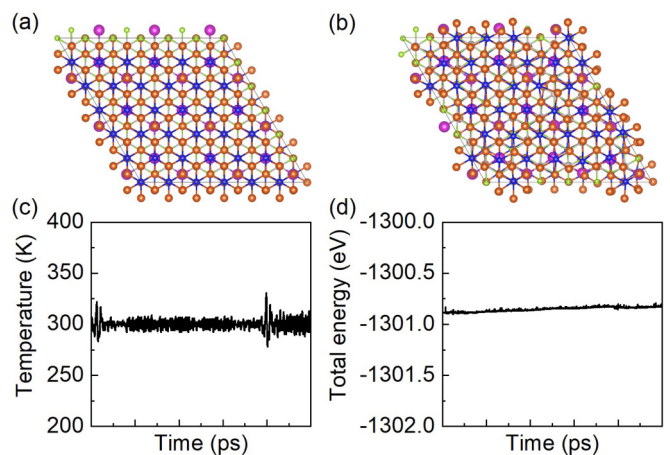


FIG. 12. The *ab initio* molecular dynamics simulations of  $\text{CoBr}_2/\text{Pt}_2\text{HgSe}_3/\text{CoBr}_2$  heterostructure. The initial structure and the structure after 5 ps of molecular dynamics simulations are shown in (a) and (b), respectively. (c) and (d) The evolution of the temperature and total energy during the molecular dynamics simulations of the heterostructure, respectively.

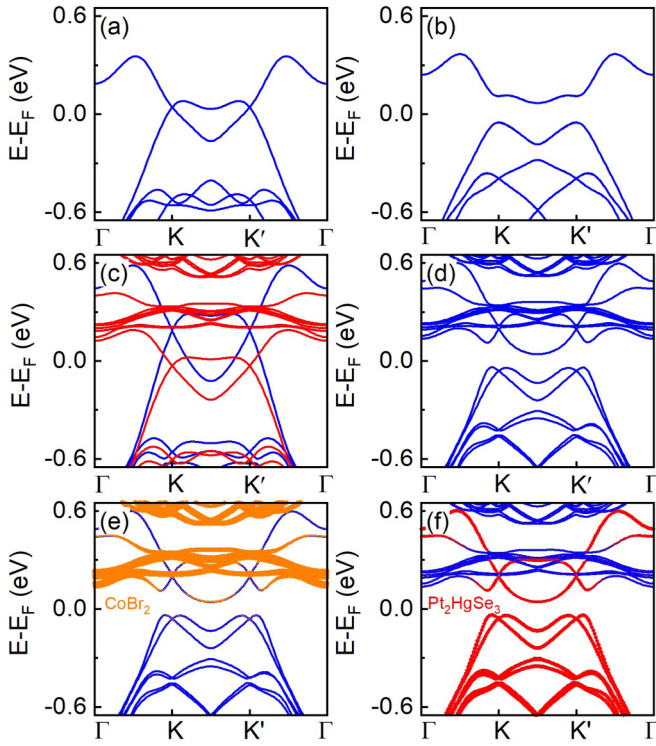


FIG. 13. The band structure evolutions of monolayer  $\text{Pt}_2\text{HgSe}_3$  and the heterostructure with/without SOC. (a) and (b) The band structure of  $\text{Pt}_2\text{HgSe}_3$  without/with SOC, respectively. (c) and (d) The band structure of  $\text{CoBr}_2/\text{Pt}_2\text{HgSe}_3/\text{CoBr}_2$  without/with SOC, respectively. (e) and (f) The orbital projections of  $\text{CoBr}_2$  and  $\text{Pt}_2\text{HgSe}_3$  on the band structure of the heterostructure.

We use the most stable configuration in our calculations (see Fig. 1). The lattice constant is  $7.35 \text{ \AA}$  for  $1 \times 1 \text{ Pt}_2\text{HgSe}_3$  and  $7.41 \text{ \AA}$  for  $2 \times 2 \text{ CoBr}_2$  which only have a small lattice difference. During the growth process,  $\text{Pt}_2\text{HgSe}_3$  and  $\text{CoBr}_2$  monolayers will slightly change their lattice constants spon-

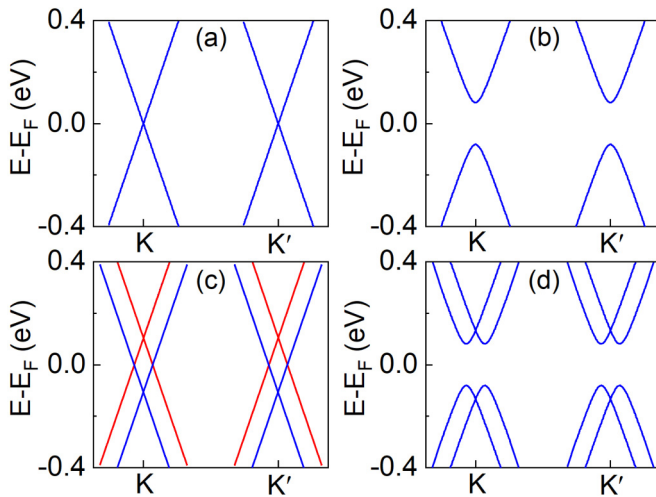


FIG. 14. The band structure of the low-energy effective model. (a)–(d) Band structure of  $H_0$ ,  $H_0 + H_{\text{soc}}$ ,  $H_0 + H_m$ , and  $H_0 + H_{\text{soc}} + H_m$ . The parameters are set as  $\hbar v_F = 1.97 \text{ eV/\AA}$ ,  $\lambda_0 = 81.2 \text{ meV}$ , and  $m_0 = 86.5 \text{ meV}$ .

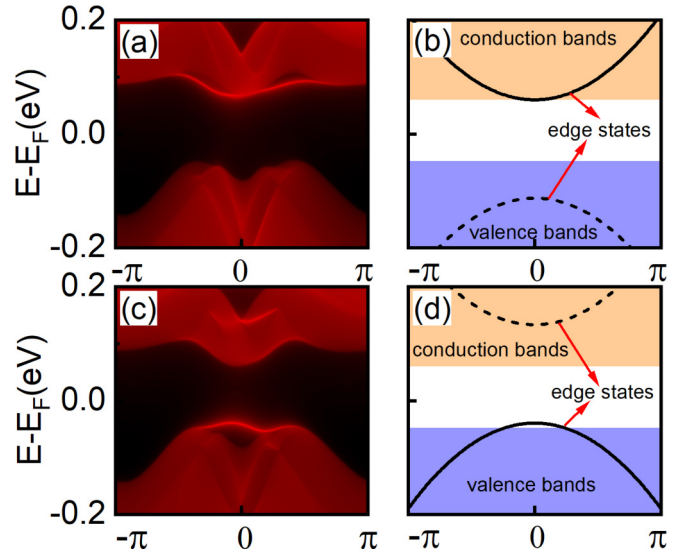


FIG. 15. The edge states of the zigzag nanoribbon and the schematic of the position of edge states. (a) and (c) The right and left edge states of the heterostructure. (b) and (d) The schematic of the position of the right and left edge states. The surface states buried in the bulk are shown as a dashed line.

taneously to match with each other. To take into account the influence of lattice constant changes, we also calculate the band structure of the heterostructure in the presence of biaxial strain. The strain can be defined as  $a = a_0(1 + \alpha)$  where  $\alpha$  and  $a_0$  represent the strain and the lattice constant of  $\text{Pt}_2\text{HgSe}_3$ , respectively. As shown in Fig. 11, we find that the tensile/compressive strain can increase/decrease the band gaps, whereas it does not obviously change the shape of band structures indicating the topological properties are not altered. As the lattice constant of  $2 \times 2 \text{ CoBr}_2$  is larger than  $\text{Pt}_2\text{HgSe}_3$ , a tensile strain stress ( $\alpha > 0$ ) is expected in this heterostructure which will increase the bulk band gap.

To verify the stability of the  $\text{CoBr}_2/\text{Pt}_2\text{HgSe}_3/\text{CoBr}_2$  heterostructure, we further perform *ab initio* molecular dynamics simulation as implemented in the Vienna *ab initio* simulation package. The canonical ensemble (NVT) was adopted for the simulations by using a Nose thermostat. We use a  $3 \times 3$  supercell of  $\text{CoBr}_2/\text{Pt}_2\text{HgSe}_3/\text{CoBr}_2$  (324 atoms) heterostructure in the simulation (non-spin-polarized calculations are performed to reduce the computational cost) with the temperature of 300 K and the time step of 1 fs. After 5000 steps

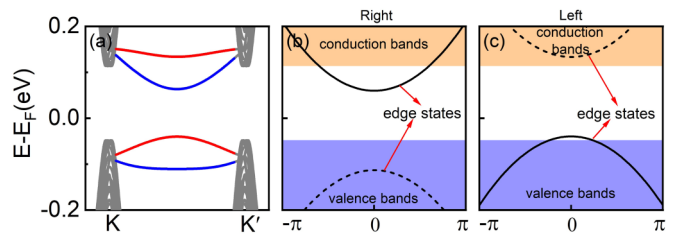


FIG. 16. The edge states of the zigzag nanoribbon from our model analyses. (a) The band structure of the zigzag nanoribbon with its right and left edge states marked by blue and red. (b) and (c) The schematic of the position of the right and left edge states.

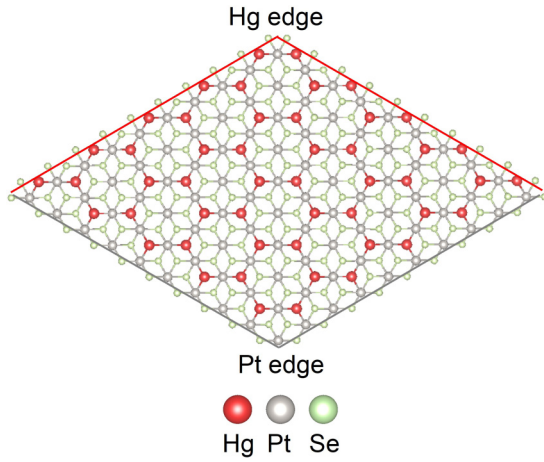


FIG. 17. The atomic structure of the  $\text{Pt}_2\text{HgSe}_3$  nanoflake. The top edges consist of Hg atoms and the bottom edges consist of Pt atoms.

(5 ps) simulation,  $\text{CoBr}_2/\text{Pt}_2\text{HgSe}_3/\text{CoBr}_2$  heterostructure preserves its respective structure as shown in Fig. 12, indicating the stability of the heterostructure.

### APPENDIX C: BAND STRUCTURE EVOLUTION OF THE HETEROSTRUCTURE AND THE LOW-ENERGY EFFECTIVE MODEL

Figures 13(a)–13(f) display the band structure evolution of  $\text{Pt}_2\text{HgSe}_3$  and its heterostructure. We plot the atomic orbital contributions of  $\text{CoBr}_2$  and  $\text{Pt}_2\text{HgSe}_3$  as shown in Figs. 13(e) and 13(f), respectively. One can find that the atomic orbitals of  $\text{Pt}_2\text{HgSe}_3$  contribute dominantly while the contributions of  $\text{CoBr}_2$  is negligible around the Fermi level. Therefore, the role

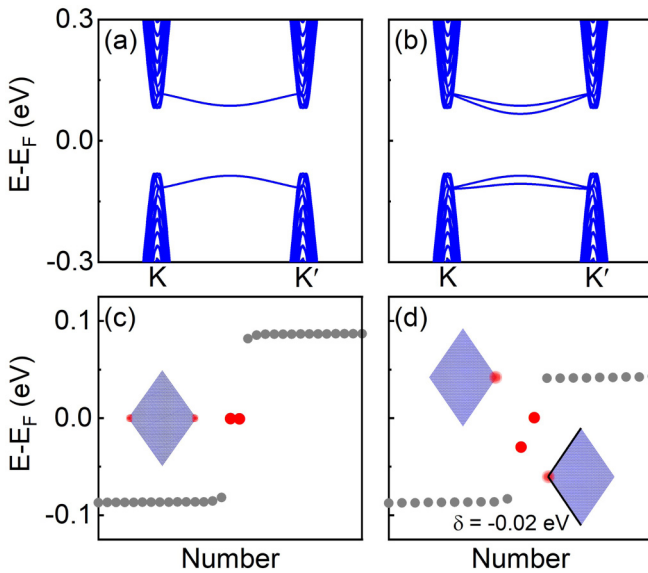


FIG. 18. The energy spectrum of the zigzag nanoribbon and zero-dimensional system without/with adding an edge potential. (a) and (c) Without edge potential. (b) and (d) With edge potential  $\delta = -0.02$  eV added on the left edge. The calculations are done by using the lattice model with parameters shown in Table I.

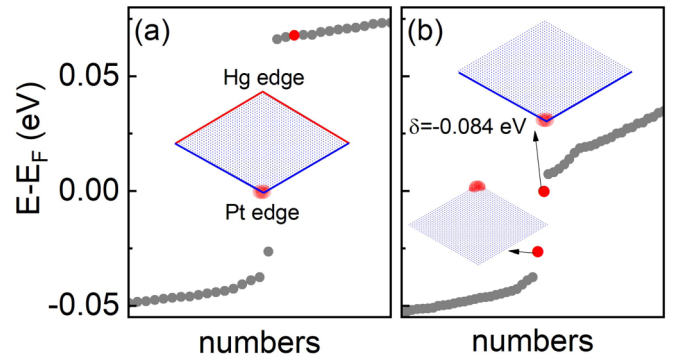


FIG. 19. Edge control of the energy spectrum of  $\text{CoBr}_2/\text{Pt}_2\text{HgSe}_3/\text{CoBr}_2$  heterostructure. (a) Without edge potential, the corner state on Pt edges is buried in bulk states. (b) With edge potentials  $\delta = -0.084$  eV added on Pt edges, the corner state is tuned to the global band gap.

of  $\text{CoBr}_2$  covering layers is mainly to introduce a sizable in-plane exchange field to  $\text{Pt}_2\text{HgSe}_3$ .

Based on the above analyses, we find that the main physics can be captured by the low-energy effective Hamiltonian as shown in Eq. (1). Figures 14(a)–14(d) show the band structure evolution of the low-energy model. We can find that the effective model and the *ab initio* band structures have the same evolution properties.

### APPENDIX D: ILLUSTRATION OF THE GAPPED EDGE STATES OF THE $\text{CoBr}_2/\text{Pt}_2\text{HgSe}_3/\text{CoBr}_2$ NANORIBBON

As shown in Figs. 15(a) and 15(c), we find that only one edge state is visible in the energy spectra of both right and left terminals. This is because the band gap of edge states is larger than the band gap of bulk states which leaves one edge state buried in the bulk states. Using the energy level of the visible edge states and the position of the corner state, we find that the gap of edge states is 173 meV. The band gap of edge states is larger than the bulk band gap (79.7 meV) which is consistent

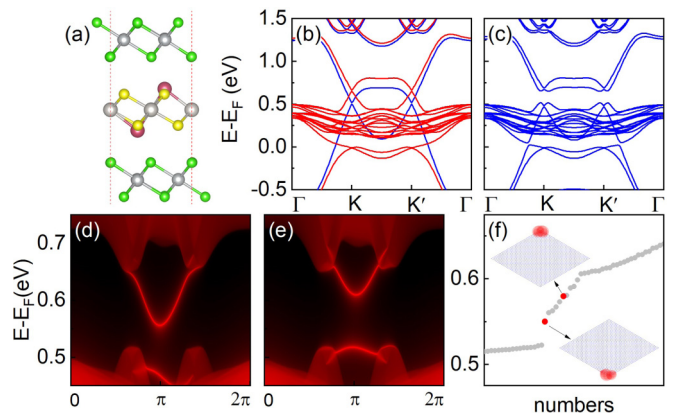


FIG. 20. The crystal structure and energy spectrums for the heterostructure of  $\text{NiCl}_2/\text{Pt}_2\text{ZnS}_3/\text{NiCl}_2$ . (a) The crystal structure. (b) and (c) The bulk band structure without and with SOC, respectively. (d) and (e) The energy spectrum of the left and right terminals, respectively. (f) Energy levels of the zero-dimension nanodisk. Corner states are highlighted in red.

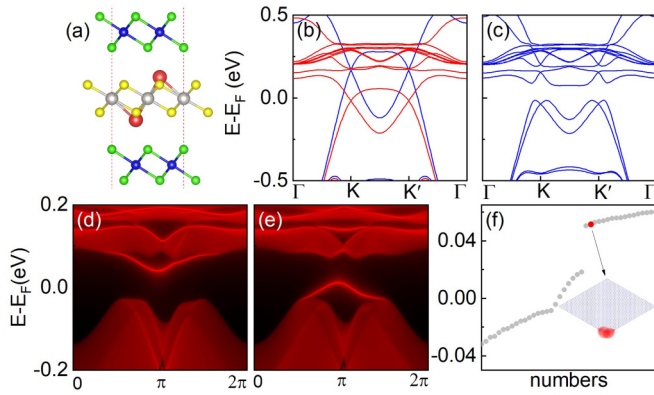


FIG. 21. The crystal structure and energy spectra for the heterostructure of  $\text{CoCl}_2/\text{Pt}_2\text{HgS}_3/\text{CoCl}_2$ . (a) The crystal structure. (b) and (c) The bulk band structure without and with SOC, respectively. (d) and (e) The energy spectrum of the left and right terminals, respectively. (f) Energy levels of the zero-dimension nanodisk. Corner states are highlighted in red.

with our previous analyses. Based on the visible edge states and the band gap of edge states, we can find the position of the edge states is illustrated in Figs. 15(b) and 15(d). The visible edge states are shown as a solid line and the invisible edge states are illustrated as a dashed line.

Then we compare it with the edge spectrum of the low-energy effective model. As shown in Fig. 16(a), we plot the band structure of the zigzag nanoribbon. On-site potential of  $-56.5$  and  $14.0$  meV are added to the right and left terminals, respectively, to simulate the effect of on-site potential differences in  $\text{CoBr}_2/\text{Pt}_2\text{HgSe}_3/\text{CoBr}_2$  heterostructure. We can see that the left and right edge bands are split up and down by the on-site potential which is consistent with our first-principles results. The relative positions of bulk states and edge states are illustrated in Figs. 16(b) and 16(c).

#### APPENDIX E: THE INFLUENCE OF EDGE POTENTIAL

For the nanoflake of  $\text{CoBr}_2/\text{Pt}_2\text{HgSe}_3/\text{CoBr}_2$  heterostructure, there are two kinds of boundaries in the supercell, which are Pt edges and Hg edges, as shown in Fig. 17. Here we use edge on-site potentials to simulate the influence of different atomic terminals. As shown in Figs. 18(a) and 18(c), there are no splitting of the edge states and corner states when no edge potential is added. In this case, the corner states distribute equally on the two corners. When edge potentials are added, the edge states are split and the two degenerate corner states

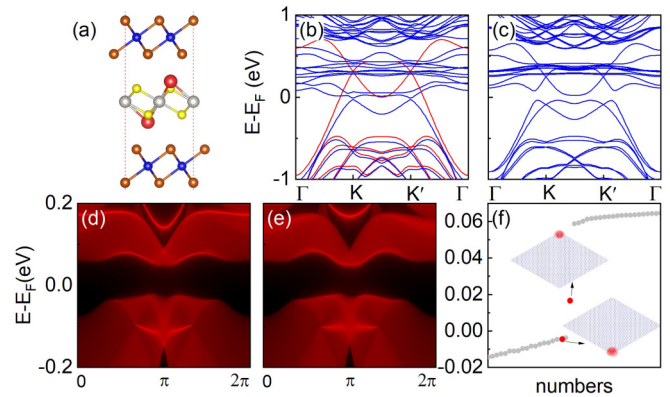


FIG. 22. The crystal structure and energy spectra for the heterostructure of  $\text{CoBr}_2/\text{Pt}_2\text{HgS}_3/\text{CoBr}_2$ . (a) The crystal structure. (b) and (c) The bulk band structure without and with SOC, respectively. (d) and (e) The energy spectrum of the left and right terminals, respectively. (f) Energy levels of the zero-dimension nanodisk. Corner states are highlighted in red.

become nondegenerate as shown in Figs. 18(b) and 18(d). In this case, the two corner states distribute on the left corner and right corner, respectively. The existence of the corner state is not affected by on-site potentials.

The corner state on the Hg edges is shown in Fig. 8(c), while the corner state on Pt edges, which is hidden in the bulk states, is displayed in Fig. 19(a). Adding negative potentials to Pt edges can tune the buried corner state to the global band gap.

#### APPENDIX F: OTHER MATERIAL CANDIDATES FOR THE SECOND-ORDER TOPOLOGICAL INSULATOR

Beside  $\text{CoBr}_2/\text{Pt}_2\text{HgSe}_2/\text{CoBr}_2$ , second-order topological states are also found in other materials in the  $\text{Pt}_2\text{HgSe}_3$  family. The electric band structures and topological properties of  $\text{MZ}_2/\text{Pt}_2\text{XS}_3/\text{MZ}_2$  ( $M = \text{Co}$  and  $\text{Ni}$ ;  $Z = \text{Br}$  and  $\text{Cl}$ ;  $X = \text{Zn}$  and  $\text{Hg}$ ) are systematically considered. Finally, we found three material candidates for second-order topological insulators which are the heterostructure of  $\text{NiCl}_2/\text{Pt}_2\text{ZnS}_3/\text{NiCl}_2$ ,  $\text{CoCl}_2/\text{Pt}_2\text{HgS}_3/\text{CoCl}_2$ , and  $\text{CoBr}_2/\text{Pt}_2\text{HgS}_3/\text{CoBr}_2$ . These monolayer magnetic substrates considered here are reported to be ferromagnetic semiconductors [45,68,69] and the GGA+ $U$  method is used with  $U = 2.13$  eV for transition metal Ni. The second-order topological states are confirmed by calculating the bulk band structures, edge states, and plot the corner states of the zero-dimensional nanodisk as shown in Figs. 20–22.

- [1] F. Zhang, C. L. Kane, and E. J. Mele, *Phys. Rev. Lett.* **110**, 046404 (2013).
- [2] W. A. Benalcazar, B. A. Bernevig, and T. L. Hughes, *Science* **357**, 61 (2017).
- [3] W. A. Benalcazar, B. A. Bernevig, and T. L. Hughes, *Phys. Rev. B* **96**, 245115 (2017).
- [4] M. Ezawa, *Phys. Rev. Lett.* **120**, 026801 (2018).
- [5] R. Chen, C. Z. Chen, J. H. Gao, B. Zhou, and D. H. Xu, *Phys. Rev. Lett.* **124**, 036803 (2020).

- [6] C. B. Hua, R. Chen, B. Zhou, and D. H. Xu, *Phys. Rev. B* **102**, 241102(R) (2020).
- [7] A. Agarwala, V. Juričić, and B. Roy, *Phys. Rev. Res.* **2**, 012067(R) (2020).
- [8] F. Schindler, A. M. Cook, M. G. Vergniory, Z. Wang, S. S. P. Parkin, B. A. Bernevig, and T. Neupert, *Sci. Adv.* **4**, eaat0346 (2018).
- [9] J. Langbehn, Y. Peng, L. Trifunovic, F. von Oppen, and P. W. Brouwer, *Phys. Rev. Lett.* **119**, 246401 (2017).

- [10] Z. Song, Z. Fang, and C. Fang, *Phys. Rev. Lett.* **119**, 246402 (2017).
- [11] M. Geier, L. Trifunovic, M. Hoskam, and P. W. Brouwer, *Phys. Rev. B* **97**, 205135 (2018).
- [12] E. Khalaf, *Phys. Rev. B* **97**, 205136 (2018).
- [13] G. van Miert and C. Ortix, *Phys. Rev. B* **98**, 081110(R) (2018).
- [14] W. A. Benalcazar, T. Li, and T. L. Hughes, *Phys. Rev. B* **99**, 245151 (2019).
- [15] F. K. Kunst, G. van Miert, and E. J. Bergholtz, *Phys. Rev. B* **97**, 241405(R) (2018).
- [16] Y. B. Yang, K. Li, L. M. Duan, and Y. Xu, *Phys. Rev. Res.* **2**, 033029 (2020).
- [17] Q. B. Zeng, Y. B. Yang, and Y. Xu, *Phys. Rev. B* **101**, 241104 (2020).
- [18] M. Ezawa, *Phys. Rev. B* **98**, 045125 (2018).
- [19] F. Liu, H. Y. Deng, and K. Wakabayashi, *Phys. Rev. Lett.* **122**, 086804 (2019).
- [20] D. Călugăru, V. Juričić, and B. Roy, *Phys. Rev. B* **99**, 041301(R) (2019).
- [21] K. Kudo, T. Yoshida, and Y. Hatsugai, *Phys. Rev. Lett.* **123**, 196402 (2019).
- [22] Y. Ren, Z. Qiao, and Q. Niu, *Phys. Rev. Lett.* **124**, 166804 (2020).
- [23] R. X. Zhang, F. Wu, and S. DasSarma, *Phys. Rev. Lett.* **124**, 136407 (2020).
- [24] L. Trifunovic and P. W. Brouwer, *Phys. Rev. X* **9**, 011012 (2019).
- [25] A. Rasmussen and Y. M. Lu, *Phys. Rev. B* **101**, 085137 (2020).
- [26] R. J. Slager, L. Rademaker, J. Zaanen, and L. Balents, *Phys. Rev. B* **92**, 085126 (2015).
- [27] R. Banerjee, S. Mandal, and T. C. H. Liew, *Phys. Rev. Lett.* **124**, 063901 (2020).
- [28] C. A. Li, S. B. Zhang, J. Li, and B. Trauzettel, *Phys. Rev. Lett.* **127**, 026803 (2021).
- [29] F. Schindler, Z. Wang, M. G. Vergniory, A. M. Cook, A. Murani, S. Sengupta, A. Y. Kasumov, R. Deblock, S. Jeon, L. Drozdov, H. Bouchiat, S. Guéron, A. Yazdani, B. A. Bernevig, and T. Neupert, *Nat. Phys.* **14**, 918 (2018).
- [30] R. Noguchi, M. Kobayashi, Z. Jiang, K. Kuroda, T. Takahashi, Z. Xu, D. Lee, M. Hirayama, M. Ochi, T. Shirasawa, P. Zhang, C. Lin, C. Bareille, S. Sakuragi, H. Tanaka, S. Kunisada, K. Kurokawa, K. Yaji, A. Harasawa, V. Kandyba *et al.*, *Nat. Mater.* **20**, 473 (2021).
- [31] X. L. Sheng, C. Chen, H. Liu, Z. Chen, Z. M. Yu, Y. X. Zhao, and S. A. Yang, *Phys. Rev. Lett.* **123**, 256402 (2019).
- [32] E. Lee, R. Kim, J. Ahn, and B. Yang, *npj Quantum Mater.* **5**, 1 (2020).
- [33] B. Liu, G. Zhao, Z. Liu, and Z. F. Wang, *Nano Lett.* **19**, 6492 (2019).
- [34] C. Chen, W. Wu, Z. M. Yu, Z. Chen, Y. X. Zhao, X. L. Sheng, and S. A. Yang, *Phys. Rev. B* **104**, 085205 (2021).
- [35] M. J. Park, Y. Kim, G. Y. Cho, and S. B. Lee, *Phys. Rev. Lett.* **123**, 216803 (2019).
- [36] B. Liu, L. Xian, H. Mu, G. Zhao, Z. Liu, A. Rubio, and Z. F. Wang, *Phys. Rev. Lett.* **126**, 066401 (2021).
- [37] C. Chen, Z. Song, J. Z. Zhao, Z. Chen, Z. M. Yu, X. L. Sheng, and S. A. Yang, *Phys. Rev. Lett.* **125**, 056402 (2020).
- [38] Y. Xu, Z. Song, Z. Wang, H. Weng, and X. Dai, *Phys. Rev. Lett.* **122**, 256402 (2019).
- [39] C. Yue, Y. Xu, Z. Song, H. Weng, Y. Lu, C. Fang, and X. Dai, *Nat. Phys.* **15**, 577 (2019).
- [40] A. K. Geim and I. V. Grigorieva, *Nature (London)* **499**, 419 (2013).
- [41] K. S. Novoselov, A. Mishchenko, A. Carvalho, and A. H. Castro Neto, *Science* **353**, aac9439 (2016).
- [42] P. E. Blöchl, *Phys. Rev. B* **50**, 17953 (1994).
- [43] G. Kresse and J. Furthmüller, *Phys. Rev. B* **54**, 11169 (1996).
- [44] J. P. Perdew, J. A. Chevary, S. H. Vosko, K. A. Jackson, M. R. Pederson, D. J. Singh, and C. Fiolhais, *Phys. Rev. B* **46**, 6671 (1992).
- [45] H. Y. Lv, W. J. Lu, X. Luo, X. B. Zhu, and Y. P. Sun, *Phys. Rev. B* **99**, 134416 (2019).
- [46] S. Grimme, *J. Comput. Chem.* **27**, 1787 (2006).
- [47] A. A. Mostofi, J. R. Yates, Y. S. Lee, I. Souza, D. Vanderbilt, and N. Marzari, *Comput. Phys. Commun.* **178**, 685 (2008).
- [48] B. Ghosh, S. Mardanya, B. Singh, X. Zhou, B. Wang, T. R. Chang, C. Su, H. Lin, A. Agarwal, and A. Bansil, *Phys. Rev. B* **100**, 235101 (2019).
- [49] J. I. Facio, S. K. Das, Y. Zhang, K. Koepernik, J. van den Brink, and I. C. Fulga, *Phys. Rev. Mater.* **3**, 074202 (2019).
- [50] I. Cucchi, A. Marrazzo, E. Cappelli, S. Ricco, F. Y. Bruno, S. Lisi, M. Hoesch, T. K. Kim, C. Cacho, C. Besnard, E. Giannini, N. Marzari, M. Gibertini, F. Baumberger, and A. Tamai, *Phys. Rev. Lett.* **124**, 106402 (2020).
- [51] K. Kandrai, P. Vancso, G. Kukucska, J. Koltai, G. Baranka, A. Hoffmann, A. Pekker, K. Kamaras, Z. E. Horvath, A. Vymazalova, L. Tapaszto, and P. Nemes-Incze, *Nano Lett.* **20**, 5207 (2020).
- [52] A. Marrazzo, M. Gibertini, D. Campi, N. Mounet, and N. Marzari, *Phys. Rev. Lett.* **120**, 117701 (2018).
- [53] A. Marrazzo, M. Gibertini, D. Campi, N. Mounet, and N. Marzari, *Nano Lett.* **19**, 8431 (2019).
- [54] A. Marrazzo, N. Marzari, and M. Gibertini, *Phys. Rev. Res.* **2**, 012063(R) (2020).
- [55] Z. Liu, Y. Han, Y. Ren, Q. Niu, and Z. Qiao, *Phys. Rev. B* **104**, L121403 (2021).
- [56] C. L. Kane and E. J. Mele, *Phys. Rev. Lett.* **95**, 146802 (2005).
- [57] B. A. Bernevig, T. L. Hughes, and S. Zhang, *Science* **314**, 1757 (2006).
- [58] R. Jackiw and C. Rebbi, *Phys. Rev. D* **13**, 3398 (1976).
- [59] F. C. de Lima, R. H. Miwa, and A. Fazzio, *Phys. Rev. B* **102**, 235153 (2020).
- [60] C. Ma, H. Forster, and G. Grundmann, *Crystals* **10**, 687 (2020).
- [61] S. N. Kempkes, M. R. Slot, J. J. van den Broeke, P. Capiod, W. A. Benalcazar, D. Vanmaekelbergh, D. Bercioux, I. Swart, and C. Morais Smith, *Nat. Mater.* **18**, 1292 (2019).
- [62] Y. Gong, J. Lin, X. Wang, G. Shi, S. Lei, Z. Lin, X. Zou, G. Ye, R. Vajtai, B. I. Yakobson, H. Terrones, M. Terrones, B. K. Tay, J. Lou, S. T. Pantelides, Z. Liu, W. Zhou, and P. M. Ajayan, *Nat. Mater.* **13**, 1135 (2014).
- [63] L. Rogée, L. Wang, Y. Zhang, S. Cai, P. Wang, M. Chhowalla, W. Ji, and S. P. Lau, *Science* **376**, 973 (2022).
- [64] L. Zhang, P. Bampoulis, A. N. Rudenko, Q. Yao, A. van Houselt, B. Poelsema, M. I. Katsnelson, and H. J. W. Zandvliet, *Phys. Rev. Lett.* **116**, 256804 (2016).
- [65] X. Li, M. Lin, J. Lin, B. Huang, A. A. Puretzky, C. Ma, K. Wang, W. Zhou, S. T. Pantelides, M. Chi, I. Kravchenko,

- J. Fowlkes, C. M. Rouleau, D. B. Geohegan, and K. Xiao, *Sci. Adv.* **2**, e1501882 (2016).
- [66] W. Dang, H. Peng, H. Li, P. Wang, and Z. Liu, *Nano Lett.* **10**, 2870 (2010).
- [67] M. Mogi, T. Nakajima, V. Ukleev, A. Tsukazaki, R. Yoshimi, M. Kawamura, K. S. Takahashi, T. Hanashima, K. Kakurai, T. H. Airma, M. Kawasaki, and Y. Tokura, *Phys. Rev. Lett.* **123**, 016804 (2019).
- [68] V. V. Kulish and W. Huang, *J. Mater. Chem. C* **5**, 8734 (2017).
- [69] M. Lu, Q. Yao, C. Xiao, C. Huang, and E. Kan, *ACS Omega* **4**, 5714 (2019).